

## ABSTRACT

Title of dissertation: Search for Pair Production of  
Third-Generation Scalar Leptoquarks  
and R-Parity Violating Stops  
in Proton-Proton Collisions at  $\sqrt{s} = 8$  TeV

Kevin Pedro, Doctor of Philosophy, 2014

Dissertation directed by: Professor Sarah C. Eno  
Department of Physics

insert abstract here

Search for Pair Production of Third-Generation Scalar Leptoquarks  
and R-Parity Violating Stops in Proton-Proton Collisions at  
 $\sqrt{s} = 8 \text{ TeV}$

by

Kevin Pedro

Dissertation submitted to the Faculty of the Graduate School of the  
University of Maryland, College Park in partial fulfillment  
of the requirements for the degree of  
Doctor of Philosophy  
2014

Advisory Committee:  
Professor Sarah C. Eno, Chair/Advisor

© Copyright by  
Kevin Pedro  
2014

## Dedication

To my parents, Philip and Lisa

## Acknowledgments

insert acknowledgments here

# Table of Contents

List of Tables	vi
List of Figures	vii
List of Abbreviations	viii
1 Introduction	1
2 Theoretical Motivations	2
2.0 The Standard Model . . . . .	2
2.1 Leptoquarks . . . . .	2
2.2 R-Parity Violating Supersymmetry . . . . .	2
3 Compact Muon Solenoid Experiment	3
3.0 The Large Hadron Collider . . . . .	3
3.1 Tracker . . . . .	3
3.2 Electromagnetic Calorimeter . . . . .	3
3.3 Hadronic Calorimeter . . . . .	3
3.4 Solenoid . . . . .	3
3.5 Muon System . . . . .	3
3.6 Trigger . . . . .	3
3.7 Luminosity Measurement . . . . .	3
4 Event Reconstruction	4
4.1 Event Generation . . . . .	4
4.2 Detector Simulation . . . . .	4
4.3 Particle Flow . . . . .	4
4.4 Tracks and Vertices . . . . .	4
4.5 Electrons . . . . .	4
4.6 Muons . . . . .	4
4.7 Jets . . . . .	4
4.8 b-tagging . . . . .	4

5	Data Analysis	5
5.1	Data Samples	6
5.1.1	Observed data	6
5.1.2	Monte Carlo	6
5.2	Selection and Optimization	6
5.2.1	Object Identification	6
5.2.2	Event Selection	6
5.3	Background Estimations	6
5.3.1	Irreducible Background (ttbar)	6
5.3.2	Reducible Background (fake tau)	6
5.3.3	Reducible Background (QCD)	6
5.3.4	Other Backgrounds	6
5.4	Systematic Uncertainties	6
5.5	Results	6
6	Calorimeter Upgrades	7
6.1	Phase 1 Simulations	7
6.1.1	HE Radiation Damage Model	7
6.1.2	Jet Studies with Radiation Damage	17
6.2	Phase 2 Simulations	17
6.2.1	Validation of Upgrade Standalone Simulation	17
6.2.2	Tests of Physics Effects on Pion Response and Resolution	17
6.2.3	HE Rebuild/Extension + Shashlik ECAL Jet Studies	17
6.3	Hadronic Fast Simulation	17
6.3.1	Retuning of Hadronic Response	17
6.3.2	MIP Fraction in Hadronic Showers	20
6.4	Dose Rate Effects	22
6.4.1	Dose Rate Effect Models	22
6.4.2	Scintillator Radiation Damage Studies	22
7	Conclusions	24
A	Full CLs Shape-Based Limits	25
B	Event Displays	26
C	Table of Monte Carlo Datasets	27
D	CMS Collaboration	28
	Bibliography	29

## List of Tables



## List of Figures

6.1	Exponential fits to 2012 HCAL laser calibration data, for layers 1 and 7 in select towers. Data for the positive (HEP) and negative (HEM) sides of the HE are shown separately. The average of the HEP and HEM values for each scaling constant $D$ is used for the radiation damage model. [1] . . . . .	8
6.2	Interpolation and extrapolation of the scaling constants $D$ for each layer of each tower in the HE. [1] . . . . .	9
6.3	Relative signal in each layer of each tower of the HE at (a) $500 \text{ fb}^{-1}$ and (b) $3000 \text{ fb}^{-1}$ . . . . .	10
6.4	Depth segmentation schemes in the HCAL for (a) Phase 0 with HPDs as the photodetectors and (b) a proposal for the Phase 1 upgrade with SiPMs as the photodetectors. Locations of the front-end electronics (FEE) for the HB and the HE are also shown. [2] . . . . .	11
6.5	Recalibration factors for the Phase 0 depth segmentation scheme. The default recalibration cutoff of 20 is shown as a dotted line on each plot. . . . .	13
6.6	Recalibration factors for the proposed Phase 1 depth segmentation scheme. The default recalibration cutoff of 100 is shown as a dotted line on each plot. . . . .	14
6.7	Plot of the SiPM dark current for different radiation doses. [2] . . . .	16
6.8	Plots of MIP percentage vs. energy for $i\eta = 1$ (in the barrel) and $i\eta = 20$ (in the endcap). . . . .	22
6.9	Plots of MIP percentage vs. energy and $\eta$ for the entire calorimeter system. . . . .	23

## List of Abbreviations

ALICE	A Large Ion Collider Experiment
APD	Avalanche Photodiode
APV	Atomic Parity Violation
ATLAS	A Toroidal LHC ApparatuS
BPTX	Beam Pick-up Timing for the eXperiments
BRW	Buchmüller-Rückl-Wyler
BSM	Beyond Standard Model
CERN	European Organization for Nuclear Research
CL	Confidence Level
CMS	Compact Muon Solenoid
CMSSW	CMS Software
CP	Charge-Parity
CPU	Central Processing Unit
CSC	Cathode Strip Chamber
CTF	Combinatorial Track Finder
DAQ	Data Acquisition
DT	Drift Tube
EB	ECAL Barrel
ECAL	Electromagnetic Calorimeter
EE	ECAL Endcap
EM	Electromagnetic
FCNC	Flavor-Changing Neutral Current
FSR	Final-State Radiation
GSF	Gaussian Sum Filter
GUT	Grand Unified Theory
HB	HCAL Barrel
HCAL	Hadron Calorimeter
HE	HCAL Endcap
HEEP	High Energy Electron Pairs
HERA	Hadron-Electron Ring Accelerator
HF	HCAL Forward
HO	HCAL Outer
HPD	Hybrid Photodiode
HLT	High-Level Trigger
IP	Interaction Point
ISR	Initial-State Radiation
L1	Level 1
L1A	Level-1 Accept
LEP	Large Electron-Positron Collider

LHC	Large Hadron Collider
LHCb	Large Hadron Collider beauty
LQ	Leptoquark
LO	Leading Order
mBRW	minimal Buchmüller-Rückl-Wyler
MB	Muon Barrel
MC	Monte Carlo
ME	Muon Endcap
MET	Missing Transverse Energy
MIP	Minimum Ionizing Particle
NLO	Next-to-Leading Order
NNLO	Next-to-Next-to-Leading Order
PD	Primary Dataset
PF	Particle Flow
PDF	Parton Distribution Function
PMT	Photomultiplier Tube
PS	Proton Synchrotron, Preshower
PSB	Proton Synchrotron Booster
QED	Quantum Electrodynamics
QCD	Quantum Chromodynamics
RBX	Readout BoX
RF	Radio Frequency
RMS	Root Mean Square
RPC	Resistive Plate Chamber
RPC	R-Parity Conserving
RPV	R-Parity Violating
SiPM	Silicon Photomultiplier
SLHA	SUSY Les Houches Accord
SM	Standard Model
SPS	Super Proton Synchrotron
SUSY	Supersymmetry
TCS	Trigger Control System
TEC	Tracker End Cap
TIB	Tracker Inner Barrel
TID	Tracker Inner Disks
TOB	Tracker Outer Barrel
TPG	Trigger Primitive Generator
TTC	Timing, Trigger and Control
VPT	Vacuum Phototriode
WLS	Wavelength-Shifting



## Chapter 1: Introduction

## Chapter 2: Theoretical Motivations

### 2.0 The Standard Model

#### 2.1 Leptoquarks

#### 2.2 R-Parity Violating Supersymmetry

## Chapter 3: Compact Muon Solenoid Experiment

### 3.0 The Large Hadron Collider

### 3.1 Tracker

### 3.2 Electromagnetic Calorimeter

### 3.3 Hadronic Calorimeter

### 3.4 Solenoid

### 3.5 Muon System

### 3.6 Trigger

### 3.7 Luminosity Measurement

## Chapter 4: Event Reconstruction

### 4.1 Event Generation

### 4.2 Detector Simulation

### 4.3 Particle Flow

### 4.4 Tracks and Vertices

### 4.5 Electrons

### 4.6 Muons

### 4.7 Jets

### 4.8 b-tagging





## Chapter 5: Data Analysis

### 5.1 Data Samples

#### 5.1.1 Observed data

#### 5.1.2 Monte Carlo

### 5.2 Selection and Optimization

#### 5.2.1 Object Identification

#### 5.2.2 Event Selection

### 5.3 Background Estimations

#### 5.3.1 Irreducible Background (ttbar)

#### 5.3.2 Reducible Background (fake tau)

#### 5.3.3 Reducible Background (QCD)

#### 5.3.4 Other Backgrounds

### 5.4 Systematic Uncertainties

### 5.5 Results

## Chapter 6: Calorimeter Upgrades

### 6.1 Phase 1 Simulations

#### 6.1.1 HE Radiation Damage Model

Radiation damage to the HE plastic scintillator tiles and wavelength-shifting fibers causes a reduction in scintillation light output. This light loss or darkening is modeled by an exponential degradation function, with specific parameters for each HE tile. These parameters were derived from 2012 HCAL laser calibration data, which exists for layers 1 and 7. Figure 6.1 shows exponential fits of relative light yield vs. integrated luminosity in  $\text{fb}^{-1}$  from the laser data for selected towers. The parameter  $D$  is a scaling constant for the exponential degradation. A smaller value of  $D$  means that the tile darkens more rapidly. The value of  $D$  varies per tile based on the pseudorapidity and layer locations of the tile, which determine the dose received, and also the size of the tile, which determines the mean path length that light must travel to escape the tile.

The scaling constants from layers 1 and 7 are interpolated for layers 2-6 and extrapolated for layers 8-17, as shown in Fig. 6.2. The values from layer 1 are used for layers 0 and -1. This specifies a radiation damage model for the entire HE.

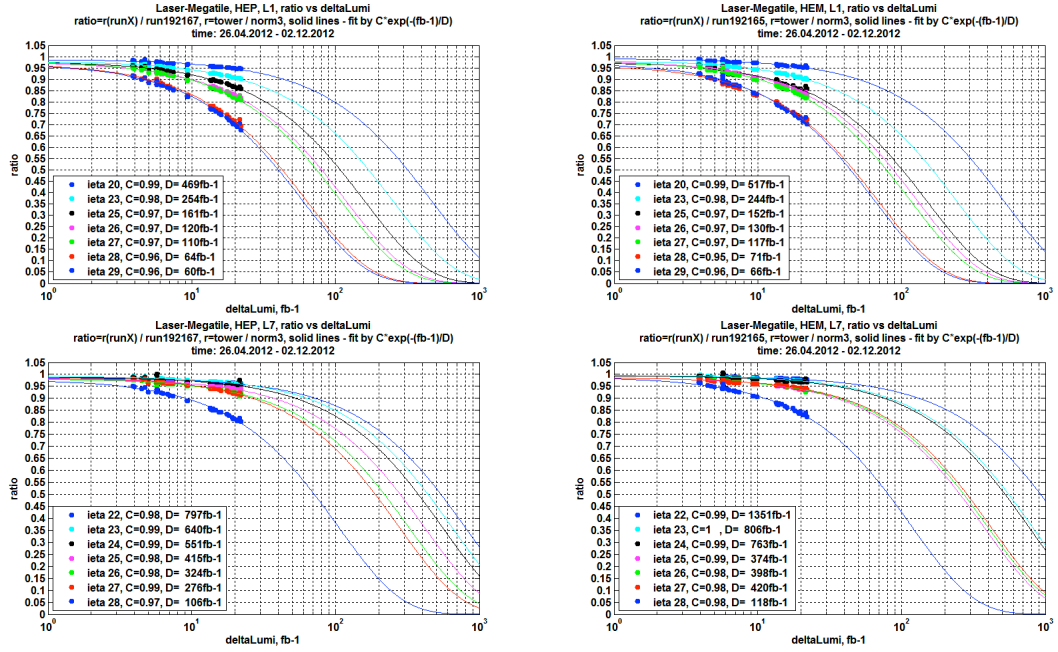


Figure 6.1: Exponential fits to 2012 HCAL laser calibration data, for layers 1 and 7 in select towers. Data for the positive (HEP) and negative(HEM) sides of the HE are shown separately. The average of the HEP and HEM values for each scaling constant  $D$  is used for the radiation damage model. [1]

Figure 6.3 shows the relative signal in each layer of each tower of the HE at different integrated luminosity values, based on this radiation damage model. When the LHC center-of-mass energy increases to 14 TeV, a given integrated luminosity value will correspond to a higher amount of dose than it would at 8 TeV when the laser calibration measurements were made. To account for this, the scaling constants are divided by a factor of 1.2, based on FLUKA calculations of the difference in particle flux for 8 TeV and 14 TeV.

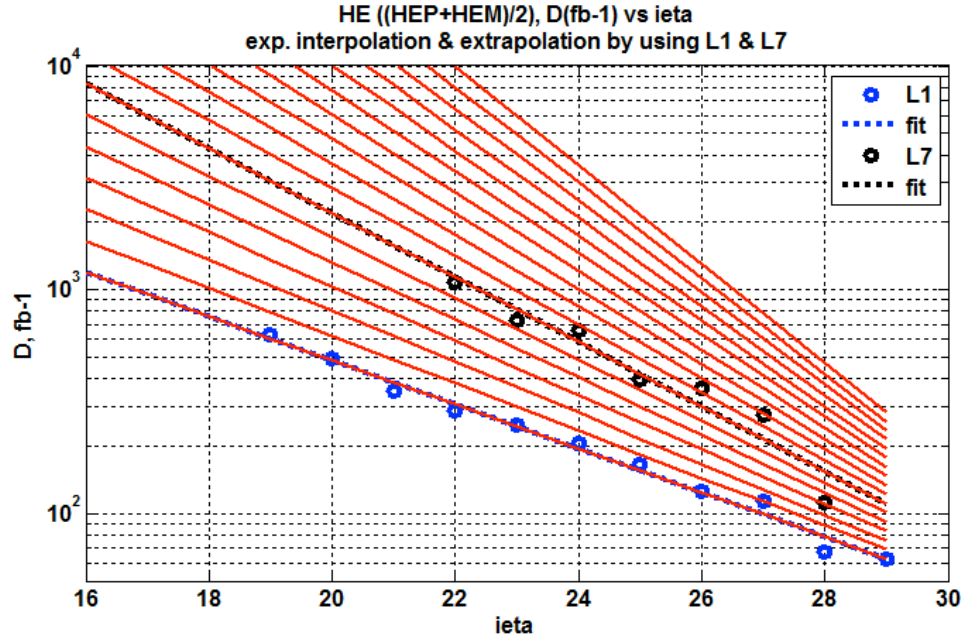


Figure 6.2: Interpolation and extrapolation of the scaling constants  $D$  for each layer of each tower in the HE. [1]

The HE photodetectors will be recalibrated to compensate for the darkening of the scintillators and fibers. In a given tower, the light output from several layers is sent to a single photodetector. Each group of layers assigned to a photodetector in this way is called a depth. The specific arrangement of layers into depths, called

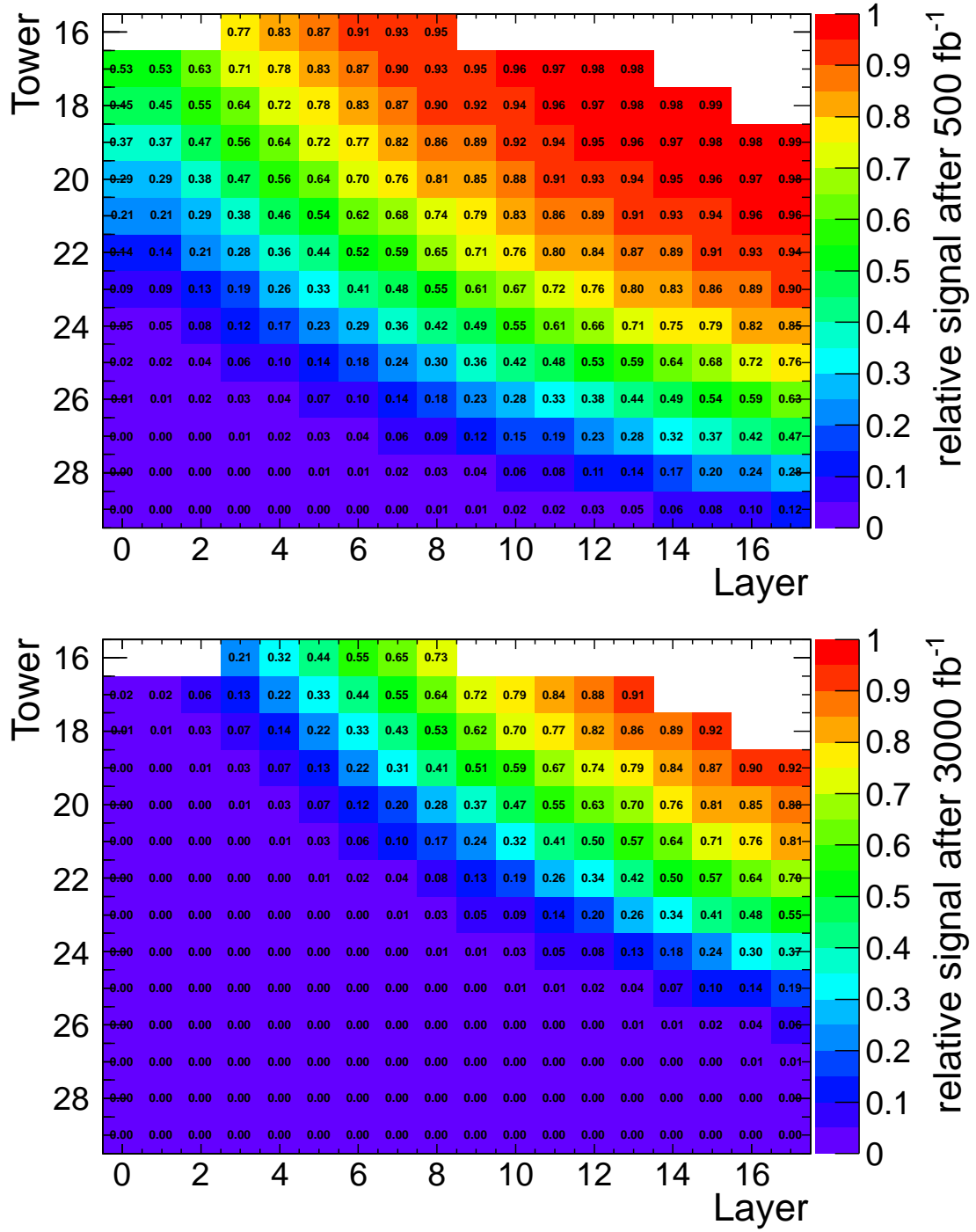


Figure 6.3: Relative signal in each layer of each tower of the HE at (a)  $500 \text{ fb}^{-1}$  and (b)  $3000 \text{ fb}^{-1}$ .

the depth segmentation scheme, will be changed during the Phase 1 upgrade of the HCAL. Figure 6.4 shows the current depth segmentation scheme and a potential upgrade scheme.

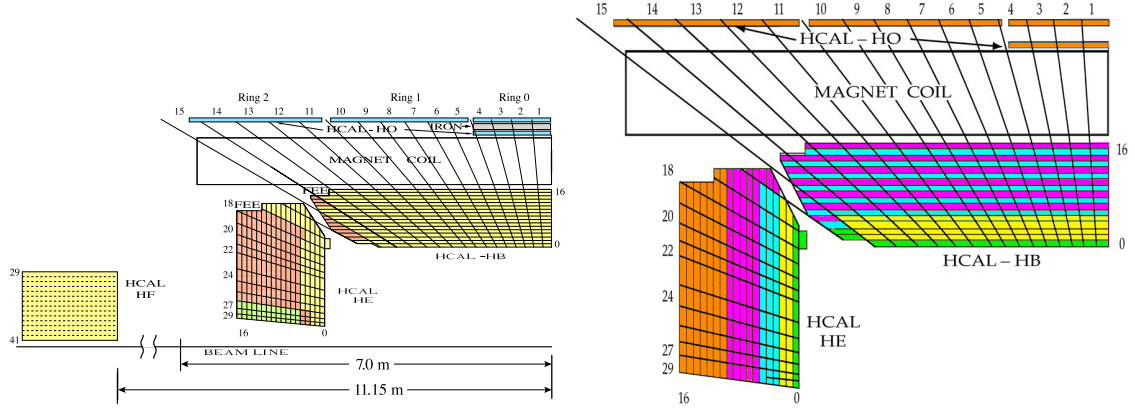


Figure 6.4: Depth segmentation schemes in the HCAL for (a) Phase 0 with HPDs as the photodetectors and (b) a proposal for the Phase 1 upgrade with SiPMs as the photodetectors. Locations of the front-end electronics (FEE) for the HB and the HE are also shown. [2]

The HE radiation damage model has a specific degradation curve for each layer of each tower. This means that recalibration factors can be calculated for any depth segmentation line scheme, as long as the initial relative weighting of layers within a depth is known. The weighting is determined by tabulating mean energy deposits  $\langle E \rangle(\ell, i\eta, 0)$  from the full simulation of 100,000 single pion events, where each pion has an energy of 50 GeV and is generated uniformly in  $1.6 < \eta < 3.0$  and in  $\phi$ . The simulation is run at  $0 \text{ fb}^{-1}$ , so no darkening is simulated. With these mean energy weights, the radiation damage model, and a depth segmentation scheme,

recalibration factors can be calculated for any integrated luminosity:

$$\langle E \rangle(\ell, i\eta, L) = e^{-L/D(\ell, i\eta)} \langle E \rangle(\ell, i\eta, 0) \quad (6.1)$$

$$\langle E \rangle(d, i\eta, L) = \sum_{\ell \in d} \langle E \rangle(\ell, i\eta, L) \quad (6.2)$$

$$f(d, i\eta, L) = \frac{\langle E \rangle(d, i\eta, 0)}{\langle E \rangle(d, i\eta, L)} \quad (6.3)$$

Equation (6.1) shows how to use the radiation damage model to find the weights at a given integrated luminosity value, based on the weights at  $0 \text{ fb}^{-1}$ . Equation (6.2) is a sum of the weights for the layers in a given depth, determined by the depth segmentation scheme. Equation (6.3) gives the calculation for the recalibration factor at a given depth and integrated luminosity. In these equations,  $\langle E \rangle$  is the average energy used as a weight (for layers or for depths),  $\ell$  is the layer number,  $i\eta$  is the tower number,  $L$  is the integrated luminosity in  $\text{fb}^{-1}$ ,  $d$  is the depth number, and  $f$  is the recalibration factor.

The recalibration factors for the specified Phase 0 and Phase 1 depth segmentation schemes are shown in Figs. 6.5 and 6.6, respectively. In practice, a maximum recalibration cutoff will be assigned so that photodetector signals and noise are not multiplied by absurdly large values. The default cutoff values are 20 for HPDs and 100 for SiPMs, shown on the figures.

Radiation does not have a large effect on the pedestal widths of the HPDs. However, the SiPMs' dark current grows with increasing radiation dose, which leads photodetector noise to increase with integrated luminosity. The simulation of SiPMs



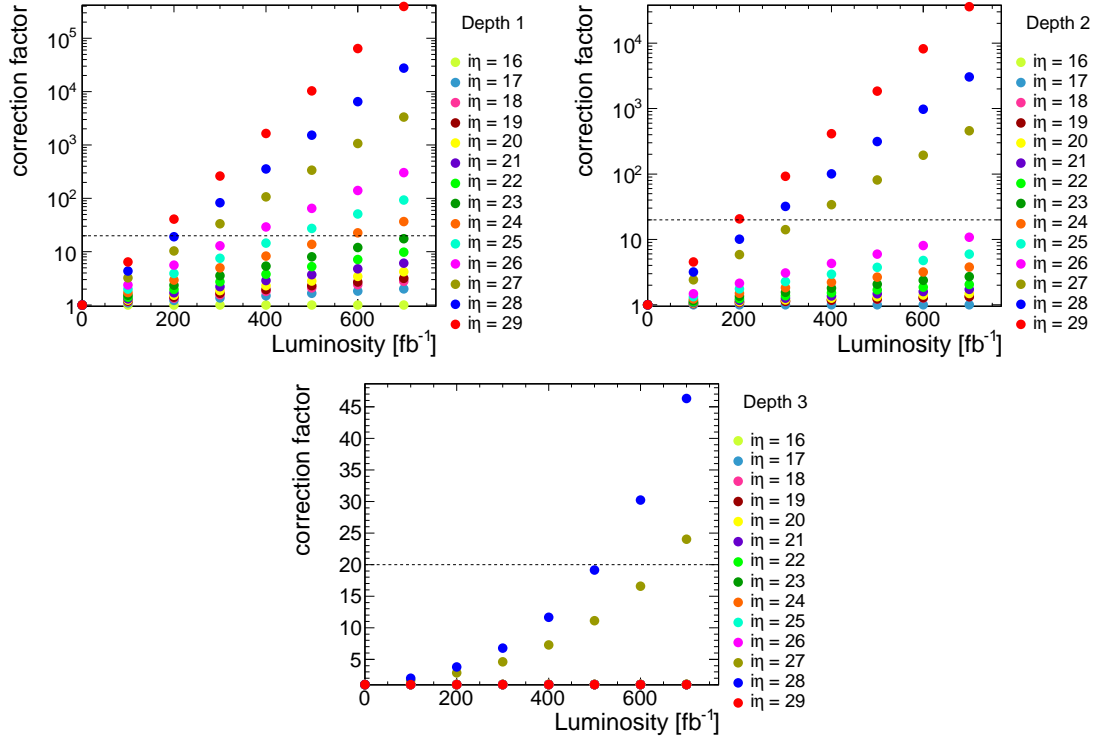


Figure 6.5: Recalibration factors for the Phase 0 depth segmentation scheme. The default recalibration cutoff of 20 is shown as a dotted line on each plot.

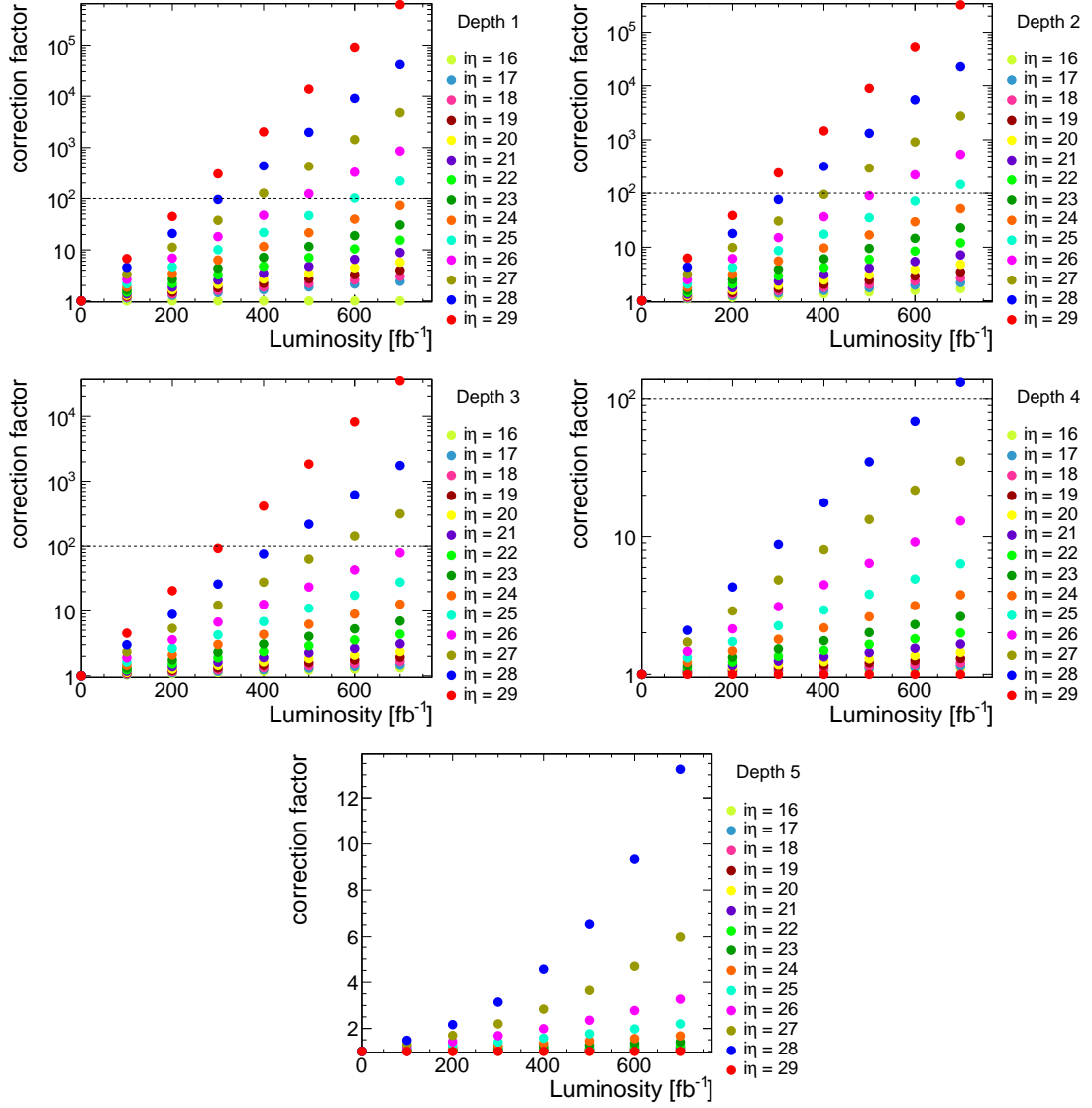


Figure 6.6: Recalibration factors for the proposed Phase 1 depth segmentation scheme. The default recalibration cutoff of 100 is shown as a dotted line on each plot.

accounts for these luminosity-dependent pedestal widths with the following equations, based on measurements shown in Fig. 6.7:

$$L_{\text{eff}} = \max(L - 200 \text{ fb}^{-1}, 0) \quad (6.4)$$

$$\sigma_{\text{SiPM}}^{(\text{HB})} = 5 + 1.7\sqrt{L_{\text{eff}}} \text{ [fC]} \quad (6.5)$$

$$\sigma_{\text{SiPM}}^{(\text{HE})} = 5 + 0.7\sqrt{L_{\text{eff}}} \text{ [fC]} \quad (6.6)$$

Equation (6.4) accounts for the planned installation of the SiPMs after  $200 \text{ fb}^{-1}$  have already been collected. Equations (6.5) and (6.6) show the scaling of the pedestal widths with the square root of integrated luminosity. The increase in dark current also changes the pedestal means and zero suppression thresholds, and the simulation accounts for these changes.

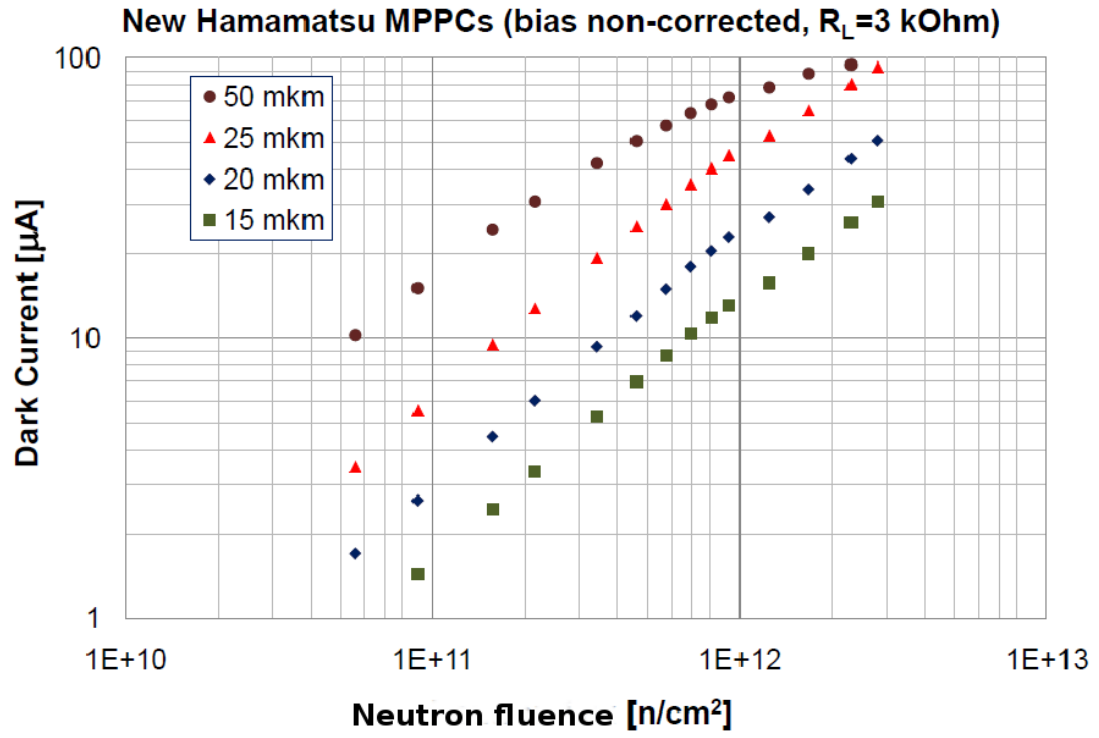


Figure 6.7: Plot of the SiPM dark current for different radiation doses. [2]

### 6.1.2 Jet Studies with Radiation Damage

## 6.2 Phase 2 Simulations

### 6.2.1 Validation of Upgrade Standalone Simulation

### 6.2.2 Tests of Physics Effects on Pion Response and Resolution

### 6.2.3 HE Rebuild/Extension + Shashlik ECAL Jet Studies

## 6.3 Hadronic Fast Simulation

### 6.3.1 Retuning of Hadronic Response

PDF and CDF definitions:

$$\int_{-\infty}^{\infty} f(x)dx = 1 \quad (6.7)$$

$$F(x) = \int_{-\infty}^x f(x')dx' \quad (6.8)$$

$$y \equiv F(x) \rightarrow F^{-1}(y) = x \quad (6.9)$$

Parameters:

$$\vec{p} = (\mu, \sigma, a_L, n_L, a_R, n_R) \quad (6.10)$$

$$d_L = n_L/a_L \quad (6.11)$$

$$d_R = n_R/a_R \quad (6.12)$$

Parameter conditions:

$$n_L, n_R > 1 \quad (6.13)$$

$$a_L, a_R > 0 \quad (6.14)$$

Normalization:

$$N = \frac{1}{\sigma \left[ \frac{d_L}{n_L-1} \cdot \exp\left(-\frac{a_L^2}{2}\right) + \sqrt{\frac{\pi}{2}} \left( \operatorname{erf}\left(\frac{a_L}{\sqrt{2}}\right) + \operatorname{erf}\left(\frac{a_R}{\sqrt{2}}\right) \right) + \frac{d_R}{n_R-1} \cdot \exp\left(-\frac{a_R^2}{2}\right) \right]} \quad (6.15)$$

Probability density function:

$$f(x; \vec{p}) = N \cdot \begin{cases} \exp\left(-\frac{a_L^2}{2}\right) \cdot \left[\frac{1}{d_L} \left(d_L - a_L - \frac{x-\mu}{\sigma}\right)\right]^{-n_L} & \text{for } \frac{x-\mu}{\sigma} \leq -a_L \\ \exp\left(-\frac{1}{2} \left(\frac{x-\mu}{\sigma}\right)^2\right) & \text{for } -a_L < \frac{x-\mu}{\sigma} < a_R \\ \exp\left(-\frac{a_R^2}{2}\right) \cdot \left[\frac{1}{d_R} \left(d_R - a_R + \frac{x-\mu}{\sigma}\right)\right]^{-n_R} & \text{for } \frac{x-\mu}{\sigma} \geq a_R \end{cases} \quad (6.16)$$

Cumulative distribution function:

$$F(x; \vec{p}) = \sigma N \cdot \begin{cases} \frac{d_L}{n_L-1} \exp\left(-\frac{a_L^2}{2}\right) \left[\frac{1}{d_L} \left(d_L - a_L - \frac{x-\mu}{\sigma}\right)\right]^{-n_L+1} & \text{for } \frac{x-\mu}{\sigma} \leq -a_L \\ \frac{d_L}{n_L-1} \exp\left(-\frac{a_L^2}{2}\right) + \sqrt{\frac{\pi}{2}} \operatorname{erf}\left(\frac{a_L}{\sqrt{2}}\right) + \sqrt{\frac{\pi}{2}} \operatorname{erf}\left(\frac{x-\mu}{\sigma\sqrt{2}}\right) & \text{for } -a_L < \frac{x-\mu}{\sigma} < a_R \\ \frac{d_L}{n_L-1} \exp\left(-\frac{a_L^2}{2}\right) + \sqrt{\frac{\pi}{2}} \operatorname{erf}\left(\frac{a_L}{\sqrt{2}}\right) \\ + \sqrt{\frac{\pi}{2}} \operatorname{erf}\left(\frac{a_R}{\sqrt{2}}\right) + \frac{d_R}{n_R-1} \exp\left(-\frac{a_R^2}{2}\right) \\ + \frac{d_R}{1-n_R} \exp\left(-\frac{a_R^2}{2}\right) \left[\frac{1}{d_R} \left(d_R - a_R + \frac{x-\mu}{\sigma}\right)\right]^{-n_R+1} & \text{for } \frac{x-\mu}{\sigma} \geq a_R \end{cases} \quad (6.17)$$

$$= \sigma N \cdot \begin{cases} B_L \left[\frac{1}{d_L} \left(d_L - a_L - \frac{x-\mu}{\sigma}\right)\right]^{-n_L+1} & \text{for } \frac{x-\mu}{\sigma} \leq -a_L \\ A_L + C_L + \sqrt{\frac{\pi}{2}} \left(1 - \operatorname{erfc}\left(\frac{x-\mu}{\sigma\sqrt{2}}\right)\right) & \text{for } -a_L < \frac{x-\mu}{\sigma} < a_R \\ A_L + C_L + C_R + A_R \\ + B_R \left[\frac{1}{d_R} \left(d_R - a_R + \frac{x-\mu}{\sigma}\right)\right]^{-n_R+1} & \text{for } \frac{x-\mu}{\sigma} \geq a_R \end{cases} \quad (6.18)$$

Inverse cumulative distribution function:

$$x = \begin{cases} \mu + \sigma \left( -d_L \left[ \frac{y}{\sigma N} / B_L \right]^{\frac{1}{-n_L+1}} - a_L + d_L \right) & \text{for } y < \sigma N A_L \\ \mu + \sigma \sqrt{2} \operatorname{erfc}^{-1} \left[ 1 - \sqrt{\frac{2}{\pi}} \left( \frac{y}{\sigma N} - A_L - C_L \right) \right] & \text{for } \sigma N A_L \leq y \leq \sigma N (A_L + C_L + C_R) \\ \mu + \sigma \left( d_R \left[ \frac{\frac{y}{\sigma N} - A_L - C_L - C_R - A_R}{B_R} \right]^{\frac{1}{-n_R+1}} + a_R - d_R \right) & \text{for } y > \sigma N (A_L + C_L + C_R) \end{cases} \quad (6.19)$$

### 6.3.2 MIP Fraction in Hadronic Showers

In the CMS hadronic shower fast simulation, the shower starting depth  $s$  is simulated using an exponential distribution. Integrate to find the cumulative distribution for inversion sampling, where  $x \in [0, 1]$  is a uniformly distributed random number:

$$f(s) = e^{-s} \quad (6.20)$$

$$F(s) = \int_0^s f(s') ds' = 1 - e^{-s} \quad (6.21)$$

$$x \equiv F(s) \rightarrow F^{-1}(x) = -\ln(1 - x) = \ln \left( \frac{1}{1-x} \right) = s \quad (6.22)$$

In the last step, the fact that  $x$  is a uniformly distributed random number in  $[0, 1]$  is used to take  $(1 - x) \rightarrow x$ .

The condition which decides if the shower will start in ECAL is based on a



comparison between the depth of ECAL  $d_{\text{ecal}}$  and the starting depth  $s$ . If the shower does not start in ECAL, the incident hadron is considered to be a MIP (minimum ionizing particle) in ECAL.

$$\frac{d_{\text{ecal}} - s}{d_{\text{ecal}}} > 0.1 \quad (6.23)$$

$$\rightarrow 0.9d_{\text{ecal}} > s \text{ (for pion showers starting in ECAL)} \quad (6.24)$$

$$\rightarrow 0.9d_{\text{ecal}} \leq s \text{ (for pions which are MIPs in ECAL)} \quad (6.25)$$

$$\rightarrow d \equiv 0.9d_{\text{ecal}} \text{ (the minimum starting distance for MIPs)} \quad (6.26)$$

Since  $f(s)$  is a probability distribution, it has area 1 in  $[0, \infty]$ . The area for  $s = d.. \infty$ , i.e. when  $s \geq d$ , should be equal to the probability  $p$  that the particle is a MIP. In order to solve this problem, the distribution must be transformed to introduce a free parameter:

$$f(s, \lambda) = \lambda e^{-\lambda s} \quad (6.27)$$

$$s = \frac{1}{\lambda} \ln \left( \frac{1}{x} \right) \quad (6.28)$$

Now the integral can be solved to require the correct MIP fraction:

$$p = \int_d^\infty ds \lambda e^{-\lambda s} = e^{-\lambda d} \quad (6.29)$$

$$\rightarrow \lambda = \frac{1}{d} \ln \left( \frac{1}{p} \right) \quad (6.30)$$

Since  $d$  is determined by detector geometry, for any  $p \in (0, 1)$ ,  $\lambda$  can be found

to ensure the correct MIP fraction. The final result is just a scaling by  $1/\lambda$  of the original equation for randomly generating  $s$  from the uniform random number  $x$ . In practice,  $p$  can be determined from full simulation as a function of incident particle energy and  $\eta$ . The easiest way to do this would be to store values for each  $\eta$  and the same energy points that are used in HCALResponse, and then interpolate for intermediate energies. (See Figures 6.8 and 6.9 for examples.) For energies outside that range, the first or last values should be used rather than extrapolating, since extrapolating could produce  $p \leq 0$  or  $p \geq 1$ , which would create unphysical values of  $\lambda$ , i.e.  $\lambda \notin (0, \infty)$ .

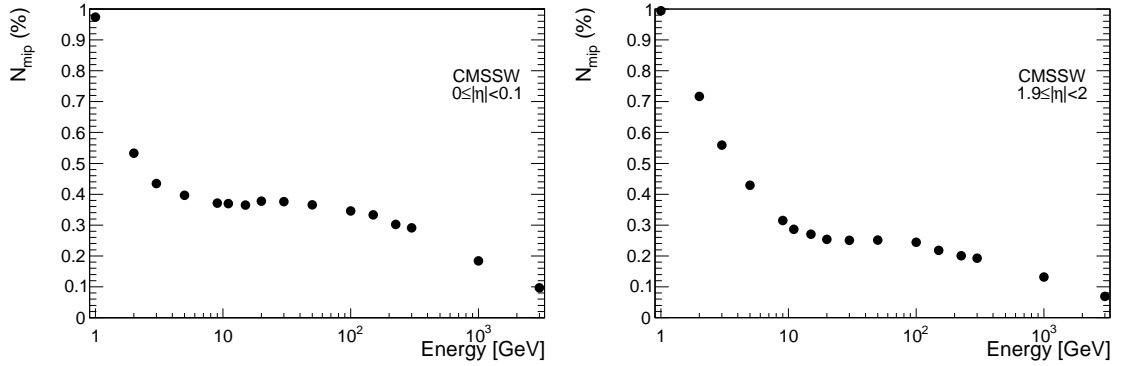


Figure 6.8: Plots of MIP percentage vs. energy for  $i\eta = 1$  (in the barrel) and  $i\eta = 20$  (in the endcap).

## 6.4 Dose Rate Effects

### 6.4.1 Dose Rate Effect Models

### 6.4.2 Scintillator Radiation Damage Studies

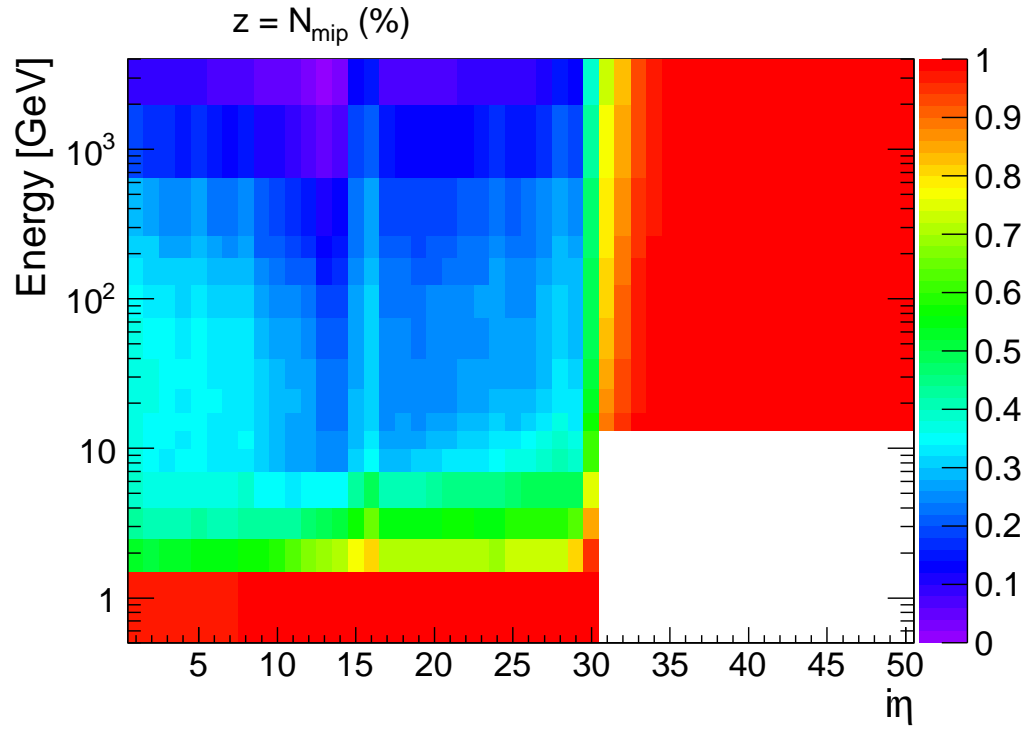


Figure 6.9: Plots of MIP percentage vs. energy and  $\eta$  for the entire calorimeter system.

## Chapter 7: Conclusions

## Appendix A: Full CLs Shape-Based Limits

## Appendix B: Event Displays

## Appendix C: Table of Monte Carlo Datasets

## Appendix D: CMS Collaboration



## Bibliography

- [1] P. de Barbaro and V. Epshteyn. <https://indico.cern.ch/contributionDisplay.py?confId=254223&contribId=1>, May, 2013. vii, 8, 9
- [2] J. Mans, “CMS Technical Design Report for the Phase 1 Upgrade of the Hadron Calorimeter”, Technical Report CERN-LHCC-2012-015. CMS-TDR-10, CERN, Geneva, Sep, 2012. vii, 11, 16